AIAA JOURNAL
Vol. 44, No. 4, April 2006

Internal Flow Temperature and Vorticity Dynamics Due to Transient Mass Addition

A. M. Hegab*
Menoufia University, Shebin El-Kom, Egypt
and
D. R. Kassoy†
University of Colorado, Boulder, Colorado 80309-0427

A model is developed for coexisting acoustic and rotational disturbances in internal flows arising from spatial distributed, transient mass addition of a constant temperature gas. The heat transfer and temperature dynamics within a channel flow are explored, in addition to the spatial distribution of the transient velocity and vorticity fields. The compressible Navier–Stokes equations are solved computationally subject to boundary conditions on the sidewalls and the exit plane, written in Navier–Stokes characteristics form to facilitate proper wave reflections. Transient solutions consist of coexisting, equal magnitude acoustics (irrotational) and vorticity as well as surprisingly large, nonacoustic transverse temperature gradients across the chamber. Results for low-Mach- and large-Reynolds-number channel flow describe spatial patterns for velocity, vorticity, temperature, and temperature gradient. The temperature gradient transient at the sidewall implies a larger amount of surface heat transfer than expected for constant temperature mass addition. The time-dependent numerical data are used to calculate the mean axial velocity distribution across the chamber and rms values for the velocity and vorticity fields to characterize flow with coexisting acoustics and vorticity. The computational solutions for a channel flow bear a strong qualitative resemblance to results obtained from an asymptotics-based modeling effort for flow in a cylinder.

Nomenclature

C = conduction operator
C_0' = speed of sound
E_T = total energy
H' = channel half-height
k' = thermal conductivity
L' = channel length
M = Mach number
n = wave number index
Pr = Prandtl number
p = pressure
q = kinetic energy
Re = Reynolds number
T = temperature
t = time
t_a' = acoustic time, L'/C_0'
U_{z0}' = reference axial speed, $\delta V_{y0}'$
u = axial speed
V = viscous operator
V_{y0}' = reference injection speed
v = transverse speed
x = axial coordinate
y = transverse coordinate
γ = ratio of specific heats
δ = aspect ratio, L'/H'
ε = injection transient amplitude
λ_n = wave number
μ = viscosity
ρ = density
Φ = dissipation operator
Ω = vorticity
ω = frequency

Subscripts and Superscripts

A = acoustic reference
p = planar quantity
r = rotational quantity
s = steady flow
t = time derivative
w = injection surface quantity
x = axial derivative
y = transverse derivative
0 = reference state
$'$ = dimensional quantity

Received 15 September 2004; revision received 1 September 2005; accepted for publication 5 October 2005.

*Professor, Department of Mechanical Power Engineering, Faculty of Engineering.
†Professor, Mechanical Engineering Department, B-427; david.kassoy@colorado.edu. Associate Fellow AIAA.

Introduction

LOW-MACH-NUMBER isothermal transient mass injection from the sidewall of a cylinder or a channel induces a time-dependent, weakly compressible high-Reynolds-number internal flow in which rotational (vorticity) and irrotational (acoustic) phenomena can coexist.[1–8] The models feature an axially distributed transverse velocity on the sidewall varying harmonically with time and a constant injected gas temperature.

Transient sidewall mass addition is the source of acoustic disturbances in the internal mean flow. An inviscid interaction between the acoustic pressure axial gradient and the injected fluid at any point on the sidewall produces a vorticity transient (axial velocity transverse gradient) there. Similarly, a significant time-dependent, temperature transverse gradient (heat transfer transient) is generated on the injection surface by a nonconductive interaction between the local acoustic temperature transient and the injected fluid.[8] Radial convection carries these surprisingly large gradients into the interior of the channel. The physical processes occurring in the interaction are transient analogues of the steady-state hard blowing phenomena discussed by Cole and Aroesty.[9] Solutions to the mathematical models,[1–8] obtained by a combination of asymptotic and computational methods, elucidate the characteristics of the acoustic disturbance, the vorticity and temperature distributions, as well as the heat transfer to the boundary.

Three broad modeling approaches have been used to study low-Mach-number, high-Reynolds-number internal mean flows with accompanying acoustic disturbances. Classical acoustic stability theory, reviewed by Culick and Yang,[10] focuses entirely on the evolution of assumed small irrotational (acoustic) velocity and pressure disturbances, to the exclusion of rotational flow (vorticity) transients. Linear analyses of models based on equations including transport effects, initiated by Flandro[11] and later reviewed by Flandro,[12] describe the evolution of small disturbances in a mean flowfield induced by steady uniform injection from the sidewall. Results describe the commensurately small vorticity transients at the injection surface, arising from an inviscid interaction between assumed acoustic pressure disturbances and the steady injected fluid, as well as the subsequent penetration of vorticity into the flowfield. Related linear studies by Majdalani and Van Moorhem,[13,14] Majdalani and Rienstra,[15] Majdalani and Flandro[16] and Flandro and Majdalani[17] are noted. More general linear stability analyses, including the effects of vorticity, are given by Casalis et al.[18] and Venugopal et al.[19,20] References 1–8 contain extensive summaries and comparisons of past related studies, including those based on computational solution methods, for example, Refs. 3, 6, and 19–25. The reader is referred to Refs. 1–8, particularly Ref. 8, for more detail.

In general, linear theories are limited to very small disturbance magnitudes. For example, Flandro's asymptotic methodology[12] implies that the magnitude of the assumed pressure disturbance is about 0.1% of the baseline pressure. In contrast, nonlinear analyses of transient flow dynamics and thermal phenomena in channel and cylinder geometries,[1–8] based on asymptotic and/or computational approaches, are valid for much larger acoustic and rotational disturbances. An initial-boundary-value problem (IBVP) approach is used to formulate the mathematical model and develop solutions. Unlike the assumed acoustic disturbances of linearized formulations, the acoustic fields in the nonlinear studies are a consequence of the specified transient mass addition boundary conditions.

More specifically, systematic asymptotic methods[1–8] are used to explain how unsteady mass addition from the sidewall of a channel or cylinder produces acoustic disturbances in the low-axial-Mach number, $M \ll 1$, high-Reynolds-number, $Re \gg 1$, mean flow. Analytical results are used to prove that the inviscid, nonconductive interactions between the acoustic transients and the time-dependent injection from the sidewall induce transverse axial velocity gradients (vorticity) and transverse temperature gradients (heat transfer) on the sidewalls.

The small axial Mach number limit, $M \ll 1$, is used to show that the nondimensional acoustic axial velocity and temperature disturbances are $\mathcal{O}(1)$ and $\mathcal{O}(M)$ quantities, respectively. In contrast, the axial velocity and temperature transverse gradients are $\mathcal{O}(1/M)$ and $\mathcal{O}(1)$, respectively. Each gradient, one order larger than the relevant disturbance itself, is attributable to the inviscid, nonconductive interaction process that is found to occur on a short radial length scale, $\mathcal{O}(MR')$, where R' represents the half-height of the channel or the radius of the cylinder.

Finally, nonlinear asymptotic modeling can be used to show that the basic velocity and pressure fields are decoupled from thermal processes.[8] It follows that the largest velocity and vorticity dynamics are not affected by temperature variations in the internal flow.

The properties of weakly compressible internal flows with coexisting acoustic and vorticity disturbances are representative of those found in the chamber of a solid rocket motor (SRM). Mass injection from the sidewall emulates product gas generation from gaseous reactant combustion in a very thin flame zone adjacent to the solid propellant. Although the feedback between the chamber flow transients and the propellant response is not included in any of the work cited thus far, the results are believed to address basic stability processes in SRMs. Recent experimental observations by Vetel et al.[26,27] support the concepts of vorticity generation featured in the modeling of Flandro and coworkers and that by Kassoy and coworkers.

Computational results in the present work describe the spatial distribution of the nondimensional temperature and vorticity transients in a channel arising from axially distributed isothermal mass addition with harmonic time dependence on the sidewall. Although the flowfield temperature disturbances themselves are small, compatible with the $\mathcal{O}(M)$ prediction of the asymptotic theory, much larger temperature gradients are present throughout the flowfield. The results are complementary to the asymptotic analysis of thermal effects in a cylinder, found in Ref. 8. In addition, they represent a refinement of the velocity and vorticity results found in Ref. 6, where thermal effects were not discussed.

Reflection-preserving numerical boundary conditions[28] are used to ensure that the computed acoustic field is an accurate solution to the posed IBVP. In particular, the present acoustic response includes eigenfunctions predicted by Staab et al.[8] as well as the forced modes seen in Ref. 6. In contrast, earlier computational results[6,21,22,24,25] include only the acoustic modes arising from the frequencies of disturbance imposed on the semiconfined system.

Results are given for a nondimensional sidewall injection distribution composed of a steady spatially uniform part and an axially distributed oscillatory part of similar magnitude. The amplitude of the latter, similar to the former, is large enough to ensure that nonlinear processes affect the evolving flowfield.[8] Nonresonant frequencies for the harmonic variation of the mass addition are the source of bounded variations in the dependent variables. Results are also given for sidewall mass addition at a near-resonant frequency for the channel geometry considered, to show how larger-amplitiude disturbances can arise.

In general, the temperature disturbance is composed of acoustic and rotational parts. The former is associated with isentropic processes in the channel. The latter, dependent on transport effects, involves nonisentropic phenomena and is sometimes referred to as an entropy wave or a transverse wave.[25,29,30] The nonlinear rotational physical phenomena occurring in the flowfield control the response of the nonisentropic part of temperature disturbance to the entire velocity field.

The observed axial variation in the radial temperature distribution is explained in terms of the acoustic-injected fluid interaction derived in the asymptotic analyses by Zhao et al.[2] and Staab et al.[5,8] Related ideas are used to show why the axial distribution of the temperature is sensitive to the axial variation in the injection velocity.

A comparison of the mean axial velocity distribution across the channel, found by averaging the time-dependent numerical data, with instantaneous values shows that the detailed structure of the latter cannot be anticipated by examining the former. In particular, relatively large oscillatory transverse velocity gradients (axial shear stresses), associated with the production of vorticity on the sidewall, cannot be inferred from the mean flow profile. Results are also given for the rms intensity of the axial velocity, composed of a purely irrotational contribution; a purely rotational contribution; and a separate mixed contribution, as well as for the Reynolds stress distribution across the channel.

Mathematical Model

The flow occurs in a narrow channel of length L' (primes denote dimensional variables), half-height H', and an aspect ratio $\delta = L'/H' \gg 1$. The pressure at the exit is prescribed whereas the closed endwall is impermeable. Inert gas, at constant temperature T_0', is injected through the porous side walls with a characteristic velocity V_{y0}', to induce an axial flow characterized by $U_{z0}' = \delta V_{y0}'$. The mathematical model is based on nondimensional Cartesian conservation equations for unsteady compressible perfect gas flow, including the parabolized form of the viscous and conduction terms (with axial transport suppressed):

$$\frac{\partial Q}{\partial t} + \frac{\partial E}{\partial x} + \frac{\partial F}{\partial y} = 0 \tag{1a}$$

where $Q = [\rho, \rho u, \rho v, E_T]^T$ and

$$E = \left\{ M\rho u,\ M\rho u^2 + (1/\gamma M)p,\ M\rho uv,\ M[E_T + (\gamma - 1)p]u \right\}^T \tag{1b}$$

$$F = \left\{ M\rho v,\ M\rho uv - (\delta^2 M/Re)u_y,\ M\rho v^2 + (\delta^2/\gamma M)p,\ M[E_T + (\gamma - 1)p]v - (\gamma \delta^2 M/Re\ Pr)T_y \right\}^T \tag{1c}$$

where E_T is the sum of the internal and kinetic energies $\{\rho[T + \gamma(\gamma-1)M^2(u^2+(v/\delta)^2]\}$. The equation of state for a perfect gas is

$$p = \rho T \tag{2}$$

It is assumed that the specific heats, the viscosity, and conductivity coefficients are constant because changes in temperature are quite small. Nondimensional variables, defined in terms of dimensional quantities denoted by a prime, are written as

$$p = p'/p'_0, \qquad \rho = \rho'/\rho'_0, \qquad T = T'/T'_0$$
$$u = u'/U'_{z_0}, \qquad v = v'\Big/\left(U'_{z_0}\Big/\delta\right)$$
$$x = x'/L', \qquad y = y'/H', \qquad t = t'/t'_a \tag{3}$$

where p'_0 is representative of the operating pressure in the chamber and T'_0 is the temperature of the injected fluid.

Characteristic length scales for the axial and transverse variables are chosen to be duct length L' and the height H', respectively. Time is nondimensionalized with respect to the axial acoustic time $t'_A = L'/C'_0$. These variables have been used in the related asymptotic analysis[8] to identify important length and timescales as well as the magnitudes of the transient variations of dependent variables.

The characteristic axial flow Mach number, Prandtl number, and flow and acoustic Reynolds numbers are defined, respectively, as follows:

$$M = U'_{z_0}/C'_0, \qquad Pr = \mu'_0 C'_{p_0}/k'_0$$
$$Re = \rho'_0 U'_{z_0} L'/\mu'_0, \qquad Re_A = Re/M \tag{4}$$

Parameter ranges of interest include $M \le \mathcal{O}(10^{-1})$, $Pr = \mathcal{O}(1)$, and $Re = \mathcal{O}(10^5$–$10^6)$. The asymptotic analyses and results in Refs. 1–8 justify the use of parabolized equations, except adjacent to the endwall.

In general, the solutions to Eqs. (1) and (2) must satisfy boundary conditions on the endwall, $x=0$; sidewall, $y=1$; centerline, $y=0$; and exit plane, $x=1$: $x=0$, $u=0$, and $T=1$; $y=1$, $u=0$, $v=v_w(x,t)$, and $T=1$; $y=0$, symmetry; and $x=1$, and $p=1$. The computational initial condition is given by $t=0$, $u=v=0$, and $p=T=1$. The pressure boundary condition at $x=1$ has been used in the related asymptotic studies to simplify the calculation of the acoustic disturbance in the channel. Other conditions imposed at the exit plane, for example, those by Landau and Lifshitz,[31] would be associated with different acoustic disturbances in the internal flow.

Numerical Method and Computational Approach

The channel flowfield time history is obtained by using a finite difference scheme capable of describing the evolution of flow variables in the axial and transverse directions after many acoustic wave cycles. The impact of numerical diffusion found to affect results obtained from a second-order explicit MacCormack code used by Kirkkopru et al.[3] is overcome by using a higher-order finite difference formulation. Adjacent to the boundaries, a second-order explicit predictor–corrector scheme, developed by MacCormack[32] is employed. At the interior points, Eqs. (1) and (2) are solved numerically using the two–four explicit predictor–corrector scheme developed by Gottlieb and Turkel,[33] which is a fourth-order variant of the fully explicit MacCormack scheme. This method is phase accurate and, therefore, suitable for describing many wave cycles and wave interaction problems.

Grid points are equally spaced in each direction within the channel. The number and spacing of the grid points used defines the accuracy and resolution of the local variations of flow variables in the axial and transverse directions. Grid point spacing is compatible with the asymptotically determined length scales discussed by Zhao et al.[2] and Staab et al.[8] The accuracy criterion for explicit schemes, introduced by Courant–Friedrichs–Lewy (see Ref. 34) and employed by MacCormack and Baldwin[35] to determine the size of the time step, is satisfied at all interior mesh points.

At the boundaries, the Navier–Stokes characteristic boundary conditions (NSCBC) technique applied by Poinsot and Lele[28] is used to specify the numerical boundary conditions that eliminate numerically generated reflected waves and to minimize the numerical dissipation near the aft end as well. [Results obtained from the two–four method with the NSCBC (see Refs. 36 and 37) technique have been compared with those from the second-order method to show that there is excess numerical diffusion in the latter.] This boundary condition formulation enables the numerical method to resolve both acoustic responses forced by the frequency of the mass addition transient and eigenfunction modes appropriate to geometry and boundary conditions.

A steady-state flow driven by constant isothermal sidewall injection is computed initially. The boundary conditions for the steady-state problem are

$$y = 1, \qquad v_s = -1, \qquad u_s = 0, \qquad T_s = 1 \tag{5}$$

$$y = 0, \qquad v_s = 0, \qquad \frac{\partial \phi}{\partial y} = 0, \qquad \phi = (u_s, \rho_s, T_s) \tag{6}$$

$$x = 0, \qquad u_s = 0 \tag{7}$$

$$x = 1, \qquad p_s = 1 \tag{8}$$

Computation time is reduced by using Culick's[38] analytical velocity profiles

$$v_{0s} = -\sin(\pi y/2) \tag{9}$$

$$u_{0s} = \pi x/2 \cos(\pi y/2) \tag{10}$$

$$(p_s - 1)/M^2 = P_{0s} = \gamma\pi^2/8(1-x^2) \tag{11}$$

as initial conditions for the steady-state computation of u_s and v_s (Ref. 39).

Numerical solutions are obtained for several values of the parameters Mach number, Reynolds number, n, and ω defined earlier. The aspect ratio $\delta = 20$ is used to describe flow dynamics in a long, relatively narrow channel, similar to that modeled with asymptotics methods.[8] The code has been run for several acoustic wave cycles to ensure that the solution converges to a steady state, defined by the condition that the total injected mass is equal to the total exiting mass and that satisfies the condition

$$\left|\phi^{t+1}_{i,j} - \phi^t_{i,j}\right| \approx 10^{-k} \tag{12}$$

where $\phi = (u, v, p, T)$ and $k \ge 4$. A comparison of Culick's steady incompressible inviscid velocity profiles, Eqs. (9) and (10), with the computed profiles for the steady compressible viscous flow is presented in Fig. 1 for $M = 0.1$, $Re = 10^5$, and $\delta = 20$. The maximum difference in the axial profiles is slightly less than 4%, whereas the transverse velocity comparison is fortuitously excellent.

The incompressible Culick solutions in Eqs. (9) and (10) represent the first asymptotic approximations in low Mach number expansions, for example, $u_s \sim u_{0s} + M^2 u_{1s} + \mathcal{O}(M^4)$, where higher-order terms describe weak compressibility effects. The 4% deviation in the centerline speed between the numerical solution and the Culick profile is comparable with the asymptotic expansion for u_s. The difference can be attributed to effects of compressibility and viscosity in the numerical solutions ignored in the Culick analyses.

The pressure solution in Eq. (11), $p_s \sim 1 + M^2 P_{0s} + \mathcal{O}(M^4)$, describes a weak compression effect due to uniform mass injection from the sidewalls. At this level of approximation, transport effects are suppressed by the large Reynolds number value. It follows that the steady flow process is approximately isentropic, and the density can be described by $\rho_s \sim 1 + M^2(P_{0s}/\gamma) + \mathcal{O}(M^2)$. The incremental increase in density implies that the average steady velocity at $x = 0.5$ will be less than that associated with the Culick profile, as will be shown later. This implication is validated by a mass balance

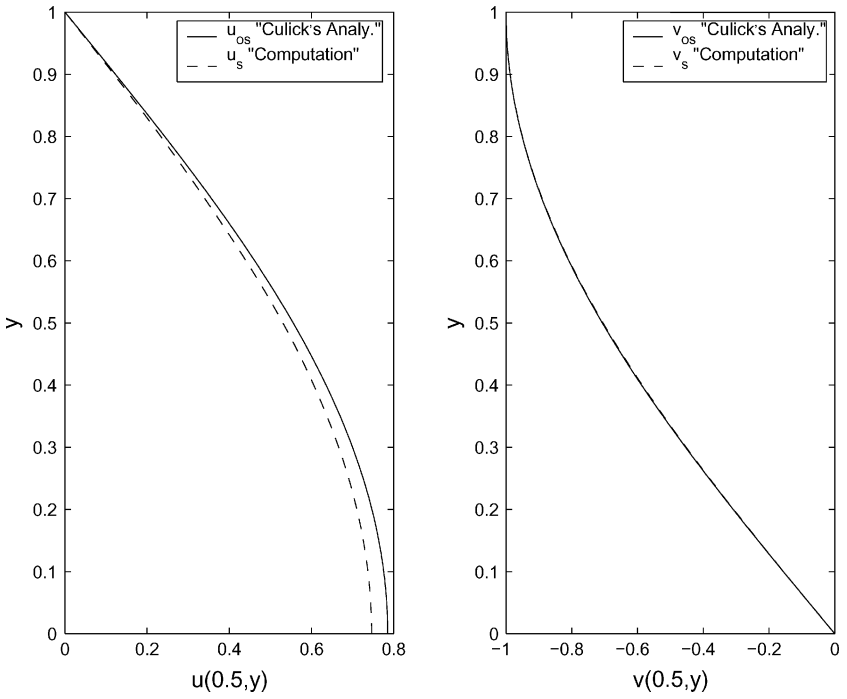

Fig. 1 Comparison of Culick's axial and transverse velocity profiles with computations at midlength of chamber for $M = 0.1$ and $\delta = 20$.

for the channel up to the axial midpoint $x = 0.5$. The results

$$\int_0^1 u_{0s}(0.5, y) = 0.5$$

$$\int_0^1 u_{1s}(0.5, y)\,\mathrm{d}y = -\frac{P_{0s}(0.5)}{2\gamma} = -3\pi^2/64 = -0.46$$

can be used with the asymptotic expansion for u_s to find

$$\int_0^1 u_s(0.5, y)\,\mathrm{d}y - \int_0^1 u_{0s}(0.5, y)\,\mathrm{d}y = -0.46M^2 + \mathcal{O}(M^4)$$

where u_s represents the numerical solution.

This difference can be compared with the area between the two curves in Fig. 1 for $M = 0.1$ to test the accuracy of the numerical result. The asymptotic prediction -0.46×10^{-2} compares favorably with the numerical difference -0.55×10^{-2} obtained from the area between the two curves in Fig. 1.

Balakrishnan et al.[40] provide a fully compressible analog to Eqs. (9–11). The small Mach number limit of their results agree with those described earlier.

The computed steady-state solution for given values of Mach number, Reynolds number, and δ is then disturbed by an unsteady sidewall injection component added to the steady value in Eq. (5). The total wall injection velocity for $t > 0$ is given by

$$v_w(x, t) = -[1 + \varepsilon \cos(\lambda_n x)(1 - \cos \omega t)], \qquad \lambda_n = n\pi/2 \quad (13)$$

where $n = 1, 3, 5, \ldots,$ to assure a net additional mass input. If $\varepsilon = 0.4$, the mean value of the injection velocity, $\bar{v}_w = [1 + \varepsilon \cos(\lambda x)]$, is always into the channel. The parameter n determines the axial wave number of the spatial variation of injection, and ω is the dimensionless angular frequency for injection time dependence. Solutions for $\omega = 1$ and 1.5 have been obtained, where the latter is a near-resonant frequency. The disturbance amplitude $\varepsilon = 0.4$ is sufficiently large to ensure that nonlinear effects influence the vorticity evolution described by Zhao et al.[2] and the radial temperature gradients discussed by Staab et al.[8] With the exception of the injection condition in Eq. (5), the remaining conditions in Eqs. (5–8) prevail. Unsteady flow computations are carried out for several different values of M and n.

Discussion of Computational Solutions

The numerical scheme is implemented to investigate the evolution of the temperature disturbances that accompany coexisting acoustic and rotational velocity disturbances in a high-aspect-ratio channel. Kirkkopru et al.[3] explain that the complete computed axial velocity field can be divided into a steady part u_s, a planar part u_p, and a rotational part u_r. The combination, $u(x, y, t) = u_r(x, y, t) + u_s(x, y) + u_p(x, t)$ is a numerical analog to the analytical division of rotational and irrotational flow discussed by Lagerstrom[30] and used subsequently by Zhao,[1] Zhao et al.,[2] Staab and Kassoy,[4] and Staab et al.[8] The quantity u_s is the solution to the steady version of Eq. (1) subject to the conditions in Eqs. (5–8). One finds the planar part by evaluating $u_p = u - u_s - u_r$ on the centerline where the condition $u_v \equiv 0$ is assumed in analogy to the low Mach number asymptotic analyses.[8] Finally, the rotational part of the velocity field is found from $u_r = u - u_s - u_p$ for any value of (x, y).

Each of the three terms u_p, u_s, and u_r is a viscous compressible analog to the velocity split derived from the low Mach number asymptotic analyses in the references just cited. With the exception of that by Kirkkopru et al.,[3,6] earlier computational studies, for example, those by Smith et al.[41] and Vuillot and Avalon,[21] do not split the numerically computed velocity. A related splitting of temperature into acoustic (isentropic) and rotational (nonisentropic) components is described by Staab et al.[8]

The total dimensionless unsteady vorticity is defined by $\Omega = -[\partial u_r/\partial y - 1/\delta^2 \partial v_r/\partial x]$ where $\Omega = \Omega'/(u'_{z_0}/H')$. The transverse speed component v_r is found from $v_r(x, y, t) = v(x, y, t) - v_s(x, y)$, where v_s represents the vertical component of the converged steady flowfield.

Solution for $n = 1$

The first case studied is for $n = 1$ and the disturbance frequencies $\omega = 1$ and 1.5. The time history for both centerline ($y = 0$) temperature and axial velocity at the midlength of the chamber, $x = 0.5$, are shown in Figs. 2 and 3, respectively, for $Re = 3 \times 10^5$, $M = 0.02$, $\delta = 20$, and $\varepsilon = 0.4$. To resolve the transverse structure of the solutions, 201 grid points were used in the y direction. Note that the bounded temperature and axial velocity solutions for $\omega = 1$, shown for about 6.5 cycles, are not merely harmonic at the forcing frequency. Rather, the results include acoustic eigenfunctions captured

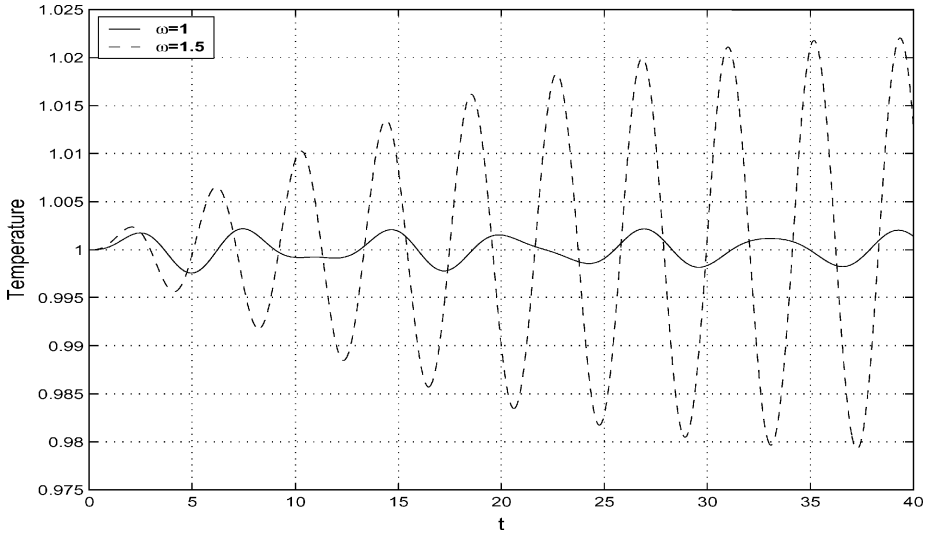

Fig. 2 Temperature time history for $\omega = 1$ and 1.5: $\varepsilon = 0.4$, $\delta = 20$, $M = 0.02$, and $Re = 3 \times 10^5$ at $x = 0.5$ and $y = 0$.

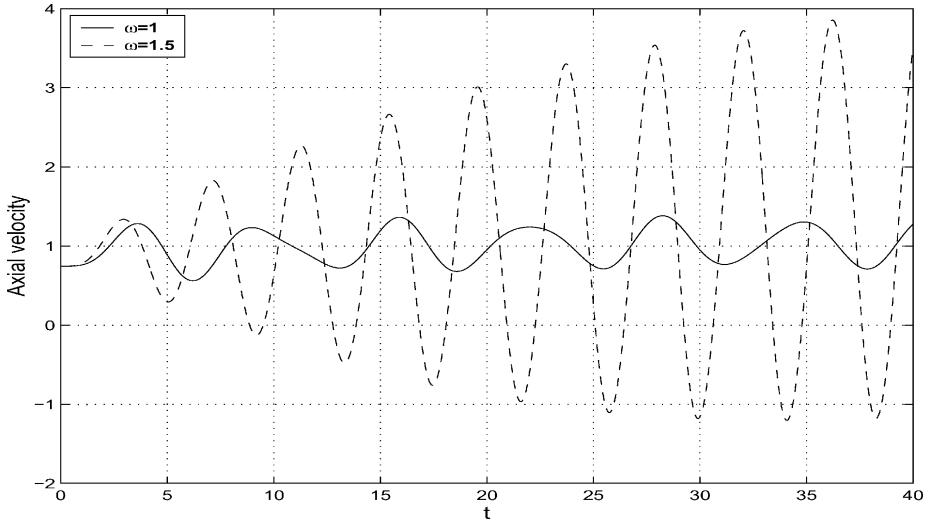

Fig. 3 Axial velocity time history with same parameters as in Fig. 2.

by using the NSCBC technique. In contrast, the Kirkkopru et al.[3,6] results show only single-frequency oscillations, probably because the numerical boundary condition treatment does not resolve wave reflection processes adequately.

An acoustic analysis[8] of Eqs. (1) and (2) with the boundary forcing in Eq. (13) can be used to show that the acoustic temperature response is described by

$$T_A \sim 1 + \frac{M(\gamma - 1)}{\gamma[(\pi/2)^2 - 1]}\left[\sin \omega t - \frac{2\omega}{\pi}\sin(\pi t/2)\right] + \cdots$$

where the first transient term arises from the imposed injection condition and the second is the relevant eigenfunction. The interaction between the former and the latter produces nonharmonic solution behavior analogous to that seen in Fig. 2. However, T_A cannot be compared directly to that result because the latter arises from a numerical solution to the complete equation system in Eq. (1).

The resonant temperature and velocity responses in Figs. 2 and 3 for the 9^+ cycle shown result from an interaction between the forced oscillation at $\omega = 1.5$ and the acoustic eigenfunction with the frequency $\nu = \pi/2$. An acoustic analysis can be used to predict a period of 4 rad compared to the computed value of about 4.02 rad. The solutions are characteristic of the front portion of a beat, where a declining growth rate of maximum amplitude with time is found.

Figure 1 shows that the steady-state axial centerline velocity at $x = 0.5$ has a value of $u(0.5, 0) \approx 0.755$ when $M = 0.1$. The analogous value for $M = 0.02$, found in Fig. 3 at $t = 0$, is $u(0.5, 0) \approx 0.778$, closer to the incompressible value of 0.785 found from Eq. (10). The responses evolve in a semiperiodic way around larger mean values, the result of the additional mean injection velocity (mass addition), represented by the term $-\varepsilon \cos \lambda_n x$ in Eq. (13).

A phase lag between the axial velocity and temperature responses is observed in Figs. 2 and 3. In other words, the temperature is not simply a passive scalar evolving in the velocity field. This is supported by the asymptotic formulation by Staab et al.[8] describing fundamental differences between the nonlinear diffusive equation for the axial velocity and that for the temperature field.

Figures 4 and 5 provide two perspectives on the spatial distribution of the complete temperature $T(x, t)$ in the channel for the parameters used in Fig. 2 at two successive times $t = 24$ and 32. At the sidewall $y = 1$, $T = 1$ is specified. At $x = 0$, the endwall temperature varies because the isothermal condition $T(0, y, t) = 1$, discussed after Eq. (4), cannot be satisfied by parabolized equations that neglect axial diffusion phenomena. A thin conductive boundary layer, as discussed in Ref. 7, is needed to complete the transition. The results show how the instantaneous temperature disturbance, generated initially along the sidewall, is convected out toward the axis $y = 0$ as time increases.

The topological structure in Fig. 4a at the time $t = 24$, contains a little less than four transverse spatial waves counting back from the edge of the ramplike surface where $y \lesssim 0.4$. The wave number

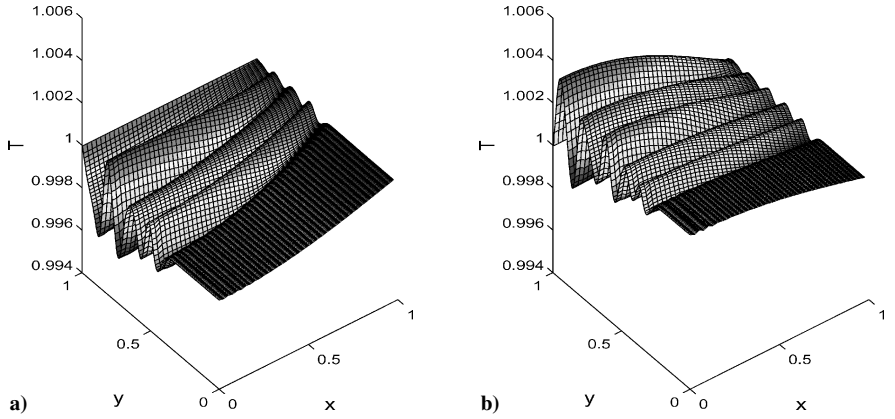

Fig. 4 Temperature topography for $\omega = 1$, $\varepsilon = 0.4$, $\delta = 20$, $M = 0.02$, $Re = 3 \times 10^5$, $n = 1$, and $\gamma = 1.4$ at $t =$ a) 24 and b) 32.

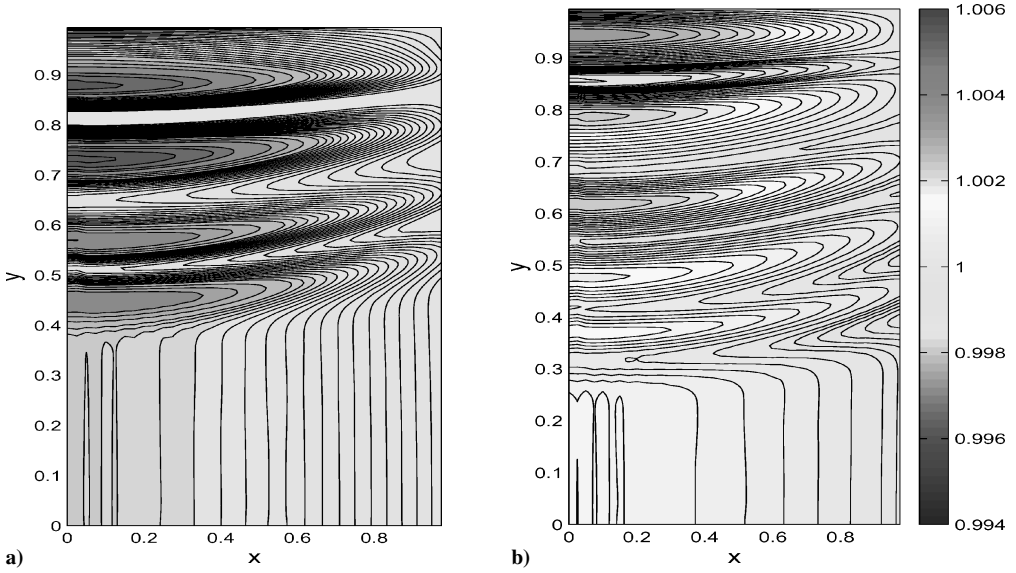

Fig. 5 Contour plot of T with same parameters as in Fig. 4.

corresponds quite nicely to the 3.82 cycles of the time dependence of the injection velocity in Eq. (13) when $\omega = 1$. Similarly, at $t = 32$ in Fig. 4b, about five spatial waves are observed, relative to 5.10 cycles of the injection speed. Staab et al.[8] have used asymptotic arguments for the limit $M \to 0$ to explain the physical characteristics of the inviscid nonconductive interaction between the acoustic pressure disturbances in the channel, generated by the transient wall velocity, and the injected fluid to produce larger than expected transverse temperature gradients at the wall. These large gradients are then convected out into the internal flow to generate the spatial structures seen in Fig. 4. Unfortunately, the asymptotic theory is developed for a long, narrow cylinder, so that quantitative comparisons with the present numerical results for a channel are not possible. However, the theory does provide qualitative validation of the present results.

Equations (1) and (2) can be used to rationalize the importance of the aforementioned interaction in the computational solution. The total enthalpy form of the energy equation can be written as

$$[\gamma/(\gamma-1)]\rho[T_t + M(uT_x + vT_y)] - p_t + (M^2/2)\Big\{(q^2)_t + M\Big[u(q^2)_x + v(q^2)_y\Big]\Big\} = [1/(PrRe)][\gamma/(\gamma-1)]\delta^2 MC + (\gamma\delta^2 M^3/Re)[\Phi + \boldsymbol{v}\cdot\boldsymbol{V}] \quad (14)$$

where $q^2 = u^2 + (v/\delta)^2$ is the kinetic energy, $\boldsymbol{V}$ is the vector viscous operator in the momentum equation, and $\boldsymbol{v}$ is the vector velocity. On the channel wall $y = 1$, the boundary conditions given after Eq. (4) must be satisfied. It follows that

$$[\gamma/(\gamma-1)](\rho v)_w(T_y)_w - [(p_t)_w/M] + (M/2)\Big[(v^2)_t + Mv(v^2)_y\Big]_w = (\delta^2/Re)\Big\{[\gamma/(\gamma-1)Pr](T_{yy})_w + \gamma M^2(\Phi + \boldsymbol{v}\cdot\boldsymbol{V})_w\Big\} \quad (15)$$

where the subscript w denotes conditions at the wall. The density $\rho \approx 1$ and $p_t = \mathcal{O}(M)$ in a transient, low-Mach-number, nearly isothermal flow.[8] The injection speed $v_w(x, t)$ is given in Eq. (13). The second term on the right-hand side of Eq. (15), the kinetic energy at the wall, is modulated by the small Mach number parameter. Finally, transport effects, represented by the last term in Eq. (15), are relatively small because $\delta^2/Re = 1.33 \times 10^{-3}$ for the parameter values used in Fig. 4. This suggests that the pressure transient $(p_t)_w/M$ dominates the right-hand side of Eq. (15). It follows that the approximation

$$(T_y)_w \approx [(\gamma-1)/\gamma v_w](p_t/M)_w \quad (16)$$

can be used to show that a nearly nonconductive interaction between the injected fluid $v_w(x, t)$ and the $\mathcal{O}(M)$-induced acoustic disturbance $p_t(x, t)$ is the source of the temperature gradient at the injection surface. This result is valid for more general acoustic disturbances than those arising in the current study based on the exit boundary condition, $p(x = 1,\ t) = 1$.

Note that the transverse wavelengths of the spatial structures in Fig. 4 are typically $\mathcal{O}(0.1)$, with some variation from wave to wave as well as transverse location. This relatively small transverse length scale is suggested by asymptotic scaling used in earlier studies.[8]

For the time values in Fig. 4, $t = 24$ and 32, the spatial wave structure ends at a well-defined transverse coordinate value for each axial location. Beyond that front location, one finds only a ramplike surface representing the purely acoustic disturbances extending to the axis $y = 0$. These ramps are similar to those predicted from analytical acoustic solutions for cylindrical geometries described by Staab et al.[8]

The same temperature fields are presented in terms of contour plots in Fig. 5 for $t = 24$ and 32, respectively. The pure acoustic field is associated with vertical contours near the centerline (bottom of Figs. 5a and 5b). The rest of Fig. 5 shows the contours associated with the spatial waves in Fig. 4. In particular, note that the transverse locations of the front and of the maximum amplitudes of the wrinkles move toward the sidewall with increasing axial location. This behavior occurs because the instantaneous injection distribution in Eq. (13) decreases monotonically downstream when $n = 1$. It follows that transverse convection at downstream locations lags that at upstream locations.

Figure 6 shows the transverse spatial variation of the instantaneous temperature across the chamber at $x = 0.5$ for the parameters in Fig. 4 when $t = 8$, 16, 24, 32, and 40. Note the spatial structures of the temperature waves out to the front representing the beginning of the pure acoustic response. These fronts move from about 0.78 for $t = 8$ to approximately 0.65 for $t = 16$, to approximately 0.38 for $t = 24$, to approximately 0.28 for $t = 32$, and to approximately 0.17 when $t = 40$. Here again, one can correlate the number of waves with the cycles of the injection velocity completed at each time value.

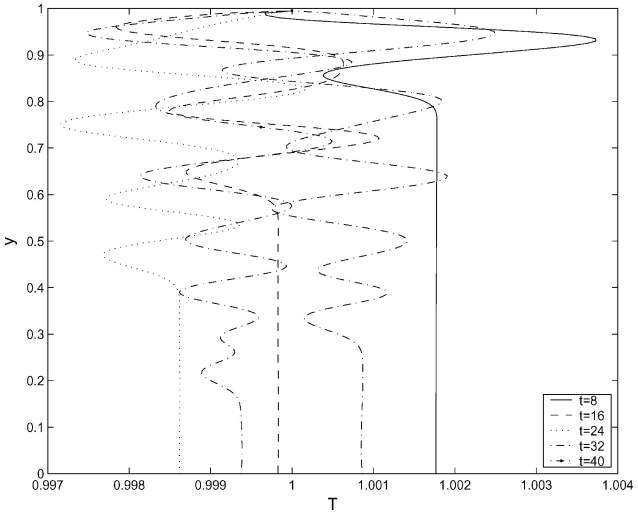

Fig. 6 Transverse variations of T for $\omega = 1$, $\varepsilon = 0.4$, $\delta = 20$, $M = 0.02$, and $Re = 3 \times 10^5$ at $x = 0.5$.

The wavelength of the spatial oscillations near the injection surface is generally larger than that away from the wall. This result, associated with the reduction in the transverse velocity as the centerline is approached, is predicted by the integral scaling technique used by Zhao[1] and Staab et al.[8] Even the smallest wavelength spatial waves in Fig. 6 have about 20 grid points per cycle, assuring adequate transverse resolution.

A surface plot of the transverse temperature gradient $\partial T/\partial y$ is shown in Fig. 7 for the same parameters as in Fig. 4 at $t = 16$ and 40. Variations in the transverse direction are more severe than those in the axial direction. The maximum amplitude of the nondimensional transverse temperature gradient is an order of magnitude larger than that of the maximum variation in the temperature shown in Fig. 4. The Staab et al.[8] asymptotic formulation implies that the temperature gradient should be one order of magnitude larger than the temperature disturbance, $T - 1$, relative to the small parameter M. The results in Figs. 4 and 5 are in excellent qualitative agreement with the analytical prediction.

The nondimensional conductive heat flux, $q = -\partial T/\partial y$, is surprisingly large, both at the wall and within the entire channel, given the small size of the temperature disturbance. A characteristic dimensional value can be written as $q' = \mathcal{O}[(k'T_0'/H')5 \times 10^{-2}]$, given the result in Fig. 7 and the definitions in Eq. (3).

The time history of the wall temperature gradient at $x = 0.5$, $\partial T/\partial y(0.5,\ 1,\ t)$, is shown in Fig. 8. This result shows that the instantaneous heat transfer at the injection surface varies significantly with time. The nonharmonic variation can be attributed primarily to the interaction represented by the approximate enthalpy equation in Eq. (15), where p_t includes both oscillations at the forcing frequency $\omega = 1$ and the eigenfrequency $\nu = \pi/2$, as described earlier for the acoustic temperature T_A.

A near-resonant temperature response is shown in Fig. 9, where $\omega = 1.5$, $Re = 3 \times 10^5$, $M = 0.02$, $\delta = 20$, and $\varepsilon = 0.4$. The largest-amplitude temperature oscillations are a factor of 10 greater than those for $\omega = 1$, due to the presence of beats (Fig. 2) when the injection velocity v_w is driven with a near-resonant frequency. One observes nearly six spatial waves at $t = 24$, compared to the 5.7 cycles of the injection velocity for $\omega = 1.5$. There are 7.6 injection cycles at $t = 32$ and nearly eight waves. These numbers exceed those found in the nonresonant situation in Fig. 4.

Figure 10 is a contour plot for the temperature when $\omega = 1.5$. Once again, the contour plots show the pure acoustic region with vertical lines. The intense black regions show regions of large transverse gradient, whereas the lightly shaded regions show regions of smaller gradients. Here again, the transverse locations of the front and of the maximum amplitude of the wrinkles move toward the sidewall with increasing axial distance downstream.

A side-by-side comparison of the nonresonant and resonant transverse temperature distributions is shown in Fig. 11 at $t = 24$ and 40 for the same parameters as in Fig. 9. The strong influence of the forcing frequency on the acoustic amplitude is noted. The front is at

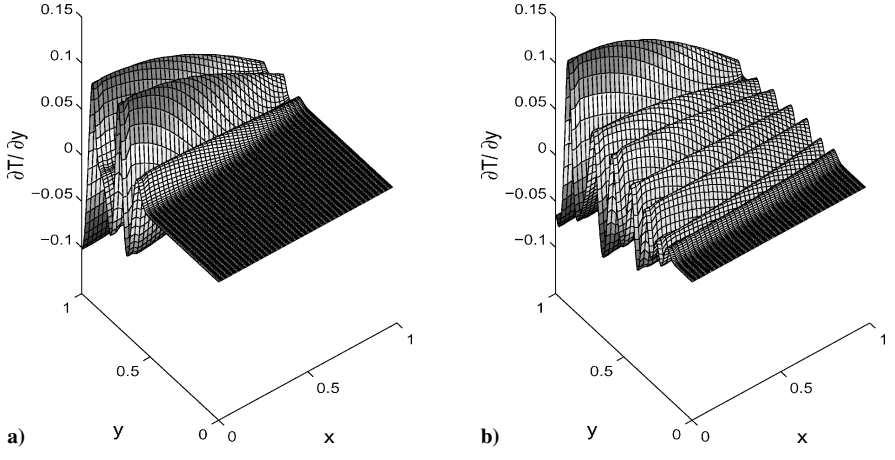

Fig. 7 Spatial distribution of temperature gradient for same parameters as in Fig. 4 at t = a) 16 and b) 40.

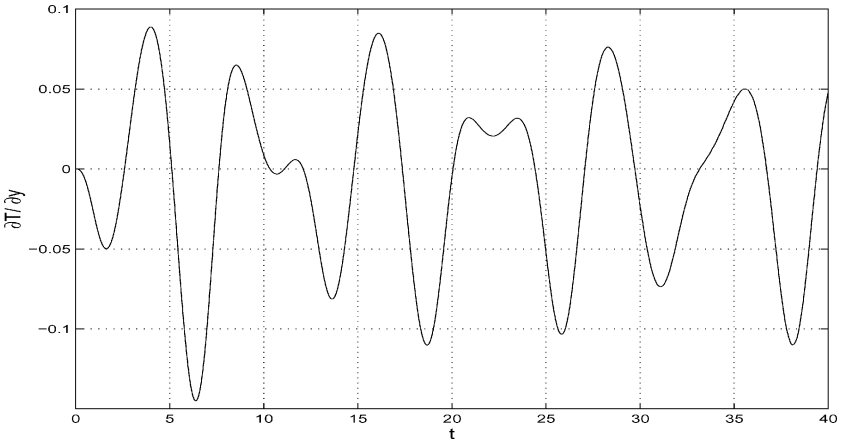

Fig. 8 Time history of wall temperature gradient at $x = 0.5$ and $y = 1.0$ with same parameters as in Fig. 4.

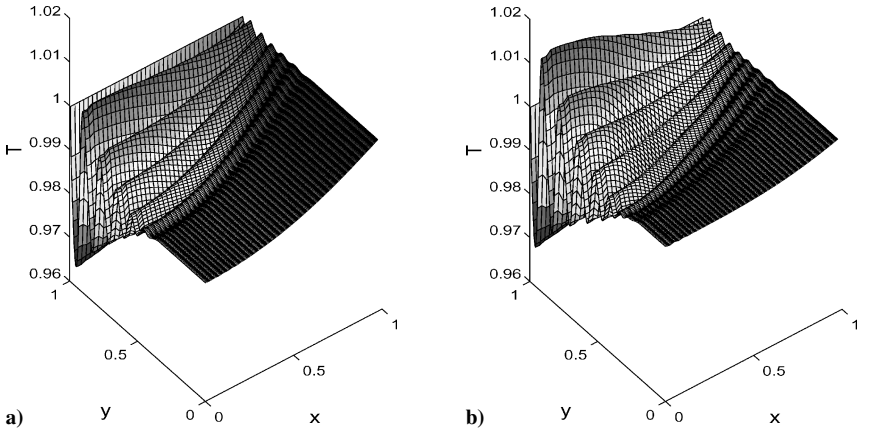

Fig. 9 Temperature topography for $\omega = 1.5$, $\varepsilon = 0.4$, $\delta = 20$, $M = 0.02$, and $Re = 3 \times 10^5$, $Pr = 1$, $n = 1$, and $\gamma = 1.4$ at $t =$ a) 24 and b) 32.

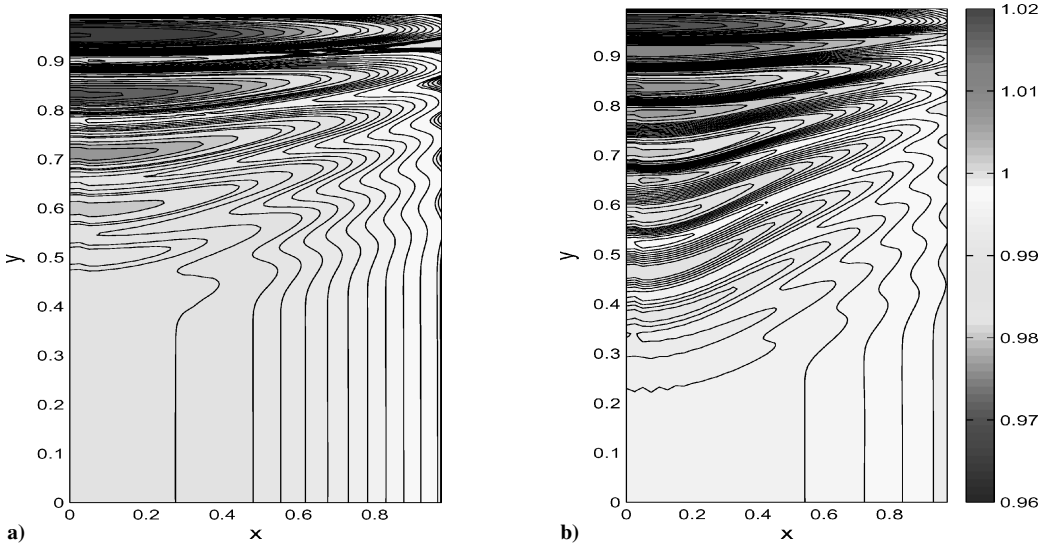

Fig. 10 Contour plot of T with same parameters as in Fig. 9.

approximately the same transverse position for both values of ω because its location is controlled primarily by transverse convection, which is not significantly affected by the imposed frequency. The value at $y = 0$ represents the purely acoustical response there.

Figure 12 shows the spatial variation of the unsteady vorticity in the channel at $x = 0.5$ and 1.0 when $t = 8$, 24, and 40 for $n = 1$, $\omega = 1$, $Re = 3 \times 10^5$, $M = 0.02$, and $\varepsilon = 0.4$. The vorticity disturbances move toward the channel centerline, $y = 0$, as time increases. For the largest time value, $t = 40$, vorticity fills about 90% of the channel. Note a little more than six wave cycles at $t = 40$ corresponding to the 6.4 oscillations in the injection speed over the time period when $\omega = 1$. As noted earlier, the wavelength of the spatial oscillations near the injection surface is generally larger than that away from the wall.

The nonlinear vorticity generation and evolution process, described in asymptotic terms in Ref. 8 can also be rationalized from Eqs. (1) and (2). Axial momentum conservation can be described by

$$\rho[u_t + M(uu_x + vu_y)] = -(1/M)(p_x/\gamma) + (\delta^2 MV/Re) \quad (17)$$

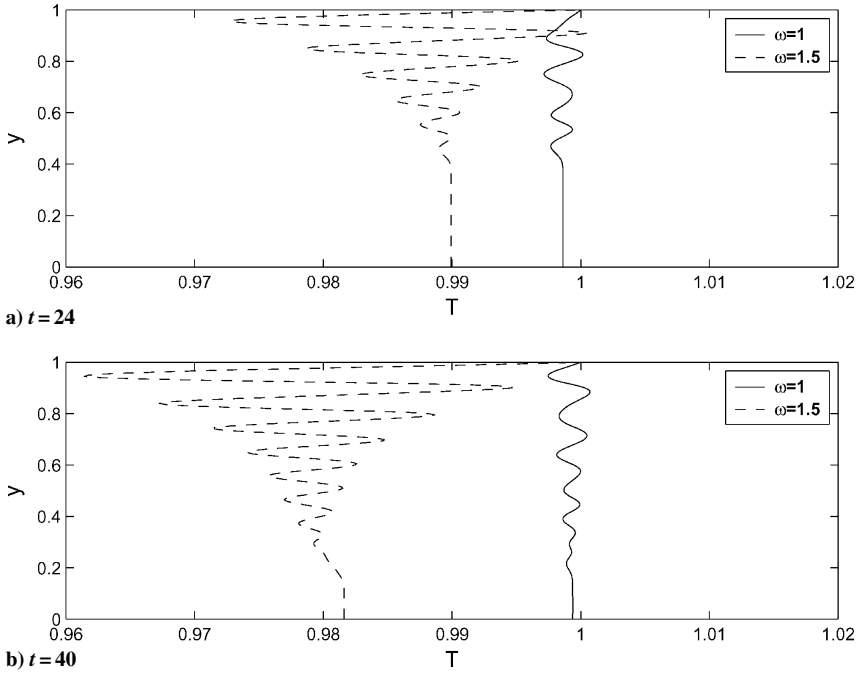

Fig. 11 Transverse variation of T for $\omega = 1$ and 1.5, $\varepsilon = 0.4$, $\delta = 20$, $M = 0.02$, $n = 1$, and $Re = 3 \times 10^5$ at $x = 0.5$.

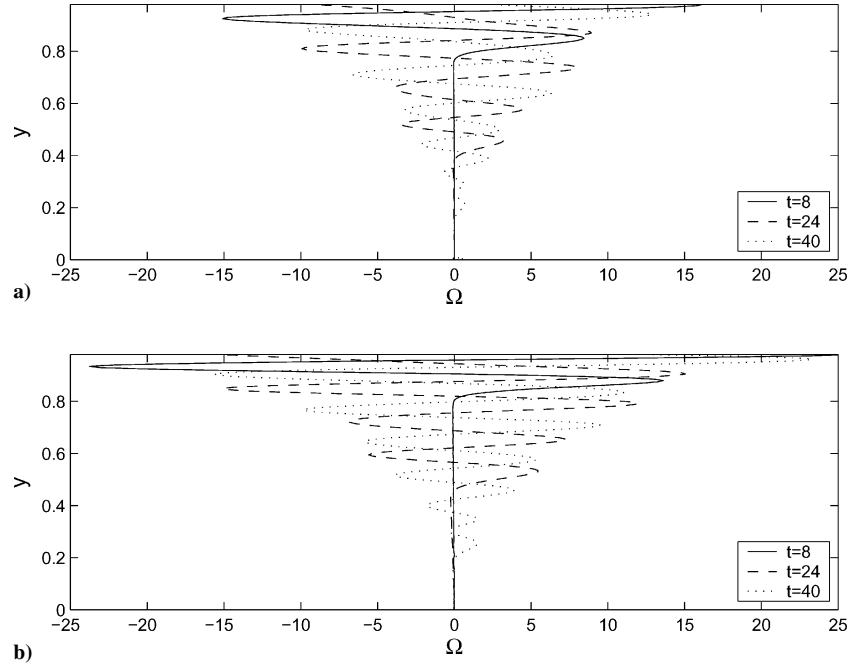

Fig. 12 Transverse variation of Ω for $\omega = 1$, $\varepsilon = 0.4$, $\delta = 20$, $M = 0.02$, $n = 1$, and $Re = 3 \times 10^5$ at $x =$ a) 0.5 and b) 1.0.

where $V(x, y, t)$ represents the axial viscous operator. On the channel wall, $y = 1$, $u(x, 1, t) = 0$, and $v_w(x, t)$, given in Eq. (13), can used in Eq. (17) to find

$$\rho_w v_w (u_y)_w = \left[-(p_x)_w/\gamma M^2\right] + \left[\delta^2 (u_{yy})_w / Re\right] \qquad (18)$$

The axial pressure gradient in this low Mach number flow is $\mathcal{O}(M)$ (Ref. 8). Given the conditions described after Eq. (15), the viscous effect is relatively small. It follows that the largest part of the vorticity on the wall is described by the approximation

$$(u_y)_w \approx -(1/\gamma M^2)[(p_x)_w / v_w] \qquad (19)$$

which is one order of magnitude in M larger than the temperature gradient in Eq. (16). This explains why the Ω amplitudes in Fig. 12 are significantly larger than the transverse temperature gradients in Figs. 7 and 8. Here again, the pressure gradient is affected by the interaction between the forced frequency response and that associated with the relevant eigenfrequency.

The absolute amplitudes of the unsteady vorticity peaks in Fig. 12b are generally larger at the exit $x = 1$ than at $x = 0.5$. This trend is predicted by the analytically derived formula for the wall vorticity $\Omega_w(x, t)$ by Staab et al.,[5] where the local amplitude of the asymptotic approximation for vorticity is found from the ratio of the local acoustic pressure gradient to the local instantaneous injection rate, a result that is analogous to that in Eq. (19). The axial derivative $\partial|\Omega_w(x, t)|/\partial x > 0$ for $n = 1$, implying that the magnitude of vorticity generated on the wall increases downstream. Because the vorticity is convected into the channel by the transverse flowfield, one may expect relatively larger values of the vorticity near the injection surface at large axial locations.

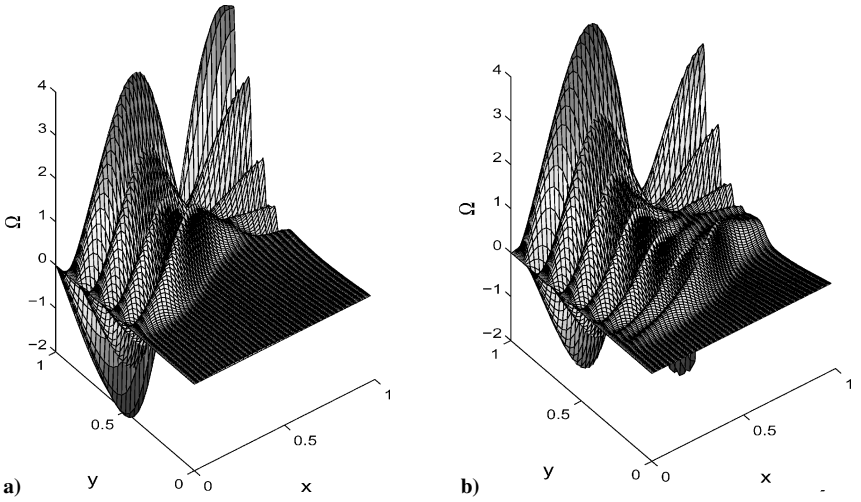

Fig. 13 Vorticity topography for $\omega = 1$, $\varepsilon = 0.4$, $\delta = 20$, $M = 0.02$, $n = 3$ and $Re = 3 \times 10^5$ at $t =$ a) 24 and b) 40.

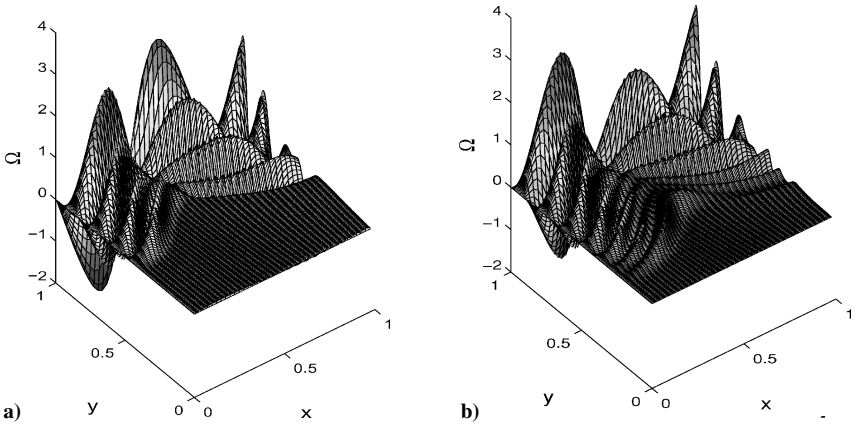

Fig. 14 Vorticity topography for $\omega = 1$, $\varepsilon = 0.4$, $\delta = 20$, $M = 0.02$, $n = 5$ and $Re = 3 \times 10^5$ at $t =$ a) 24 and b) 40.

At the exit, $x = 1$, the magnitude of the vorticity close to the injection surface can be larger than 20 for the example with $M = 0.02$. The asymptotic analyses by Staab et al.[5,8] and Zhao et al.[2] show that the vorticity is $\mathcal{O}(1/M)$, which is certainly qualitatively compatible on a magnitude basis with the results found in the present work.

Solutions for $n = 3$ and 5

Solutions can be found for odd values of the integer n in Eq. (13) to examine the effect of larger wave number distributions of net positive mass injection. The vorticity distributions in the channel for $n = 3$ and 5 are shown in Figs. 13 and 14 for $t = 24$ and 40. The 40 grid points used in the axial direction are sufficient to resolve the axial spatial structure for $n = 3$ and 5.

The complexity of axial variations in the spatial waves is enhanced as the wave number index n is increased from 3 to 5. Additional axial spatial waves are seen for $n = 5$ in Fig. 14. In addition, the shapes of the vorticity fronts at $t = 40$, for $n = 3$ and 5, are quite different. These results suggest that the spatial distribution of mass injection can have a significant impact on the characteristics of vorticity in the channel.

A comparison of the results with those in Fig. 12 shows that the maximum characteristic amplitude of the vorticity peaks decrease with increasing value of n. The explanation for this dependence can be obtained from Eq. (19) and the properties of the embedded acoustic field.[8] In particular, the acoustic pressure gradient for $\omega = 1$ is described by

$$\frac{p_x}{M} = -\frac{(n\pi/2)}{[(n\pi/2)^2 - 1]}\left[\sin t - \frac{\sin(n\pi/2)t}{(n\pi/2)}\right]\sin(n\pi/2)x$$

$$n = 1, 3, 5, \ldots$$

where the first term in the transient represents a forced response and the second is associated with the eigenfrequency. Note that the amplitude of the pressure gradient decreases with n, and the relative importance of the eigenfrequency effect decreases with n. It follows from Eq. (19) that the amplitude of the induced vorticity will decrease with increasing values of n. This implies that vorticity generation will be relatively small when the wave number of the injection transient in Eq. (13), $\lambda_n = n\pi/2$, is sufficiently large.

Vorticity contour plots for $n = 1, 3$, and 5 when $\omega = 1$ are shown in Figs. 15–17 at $t = 24$ (Figs. 15a, 16a, and 17a) and 40 (Figs. 15b, 16b, and 17b). At each time value, the number of transverse structures is the same for $n = 1$, 3, and 5. However, the axial structures are quite different. Note that the transverse penetration of vorticity into the channel is minimized at the axial location of the minimum in the wall injection velocity in Eq. (13). This result is expected because the penetration is related to the local radial convection speed.[8]

For $n = 1$ in Fig. 15, the contours show several spatial waves of vorticity across the channel with largest value (darkest shading) near the sidewall. The peak amplitude increases, and the location of the peaks moves toward the sidewall with increasing axial distance downstream. The largest shear stresses appear at the downstream locations for $n = 1$. The peak results described by Liou and Lien[42] and Kirkkopru et al.[3,6] are qualitatively similar for the case $n = 1$.

For $n = 3$ and 5 in Figs. 16 and 17, many of the Ω contours are closed. When one moves axially along a vorticity cell structure, there is a nonmonotonic amplitude variation with distance downstream. The transverse location of the vorticity varies considerably in the downstream direction. In addition, the variation in the front location with increasing axial distance is not monotonic as in Fig. 15 for $n = 1$. The difference arises from the nonmonotonic spatial variation of the injection speed in Eq. (13) for $n = 3$ and 5 compared to the

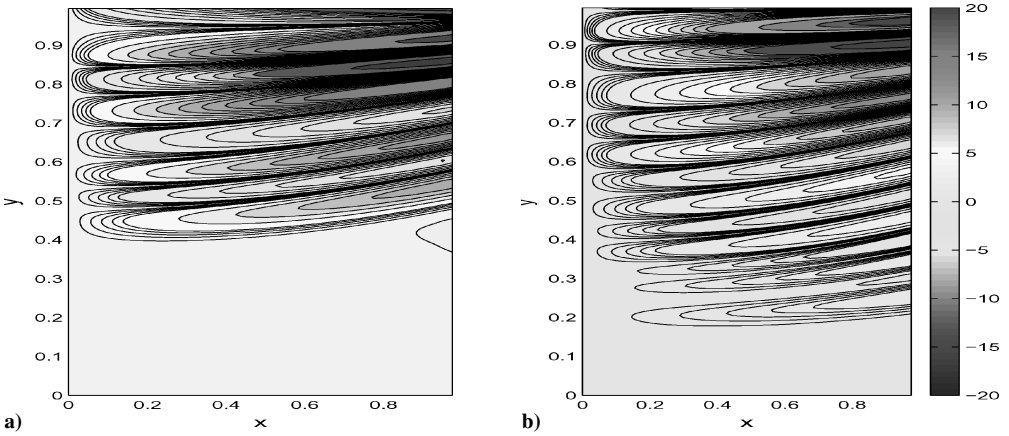

Fig. 15 Contour plot of Ω with same parameters as in Fig. 12 for $n = 1$.

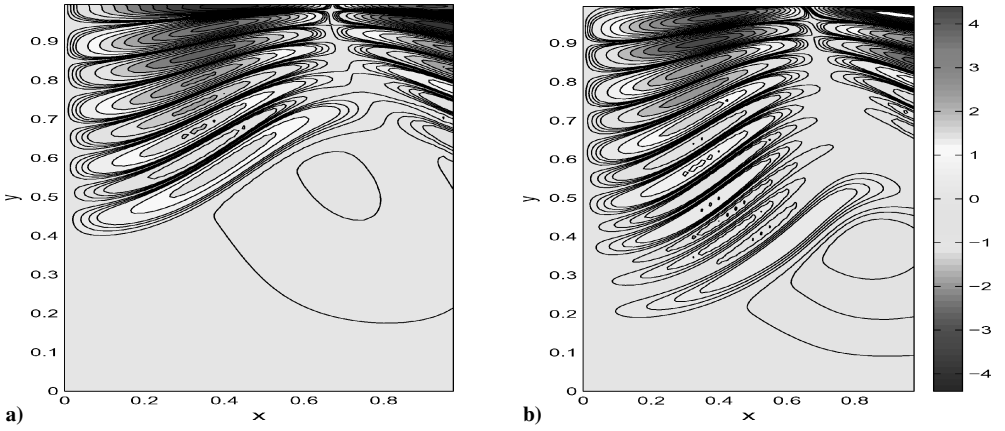

Fig. 16 Contour plot of Ω with same parameters as in Fig. 12 for $n = 3$.

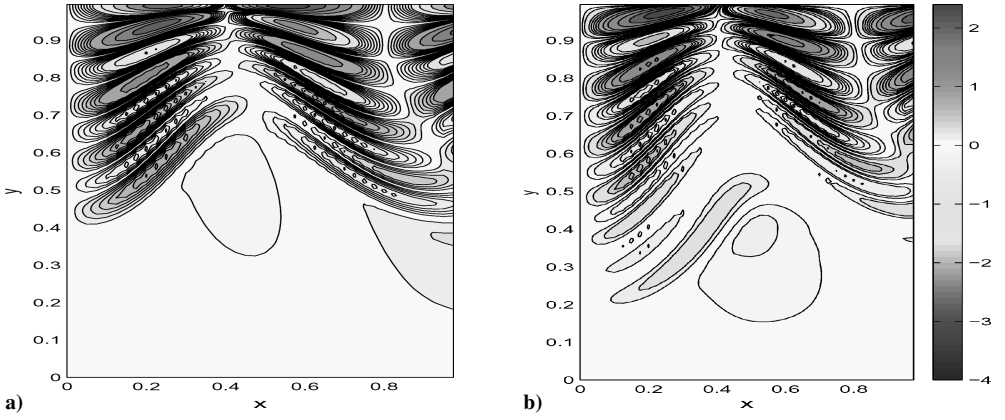

Fig. 17 Contour plot of Ω with same parameters as in Fig. 12 for $n = 5$.

monotonic decrease for $n = 1$. In fact, the changes in alignment of the vorticity structures in Figs. 16 and 17 are similarly related to the spatial variation of the injection speed.

The intense black regions of concentrated contours show the relatively large absolute magnitude of the vorticity near the wall, whereas the lighter portions represent smaller variations near the centerline. The decrease in the maximum amplitude of Ω as the wave number index n increases is noted once again.

Mean and Fluctuating Flow Properties

The computational results by Liou and Lien[42] and the linear stability theory of Casalis et al.,[18] both for channel flows with constant, spatially uniform wall injection, imply that hydrodynamic instability will not be an important factor when the Reynolds number defined in Eq. (4) $Re = 3 \times 10^5$. Given that the aspect ratio $\delta = 20$, the corresponding channel Reynolds number $Re_c = V'_{y0}H'/\nu = 750$. In this regard, the steady flow configuration should be stable, with a relatively low level of vorticity associated with the profile in Fig. 1.

A formal stability theory with imposed transient sidewall mass addition does not appear to have been attempted. On the other hand, the asymptotic studies summarized in Ref. 8 and that by Hegab et al.[43] are initial-value analyses that should, in principle, be able to predict the complete time history of a channel flow with transient mass addition if the spatial and time resolutions are sufficiently fine. Numerical solutions of the asymptotically reduced equations[8] exhibit the same flow characteristics found in the present fully computational solutions. The former do not suggest that a hydrodynamical instability is occurring in the flow. One may reasonably conclude that the vorticity and transverse temperature gradient generation mechanisms discussed earlier are the only sources of relatively

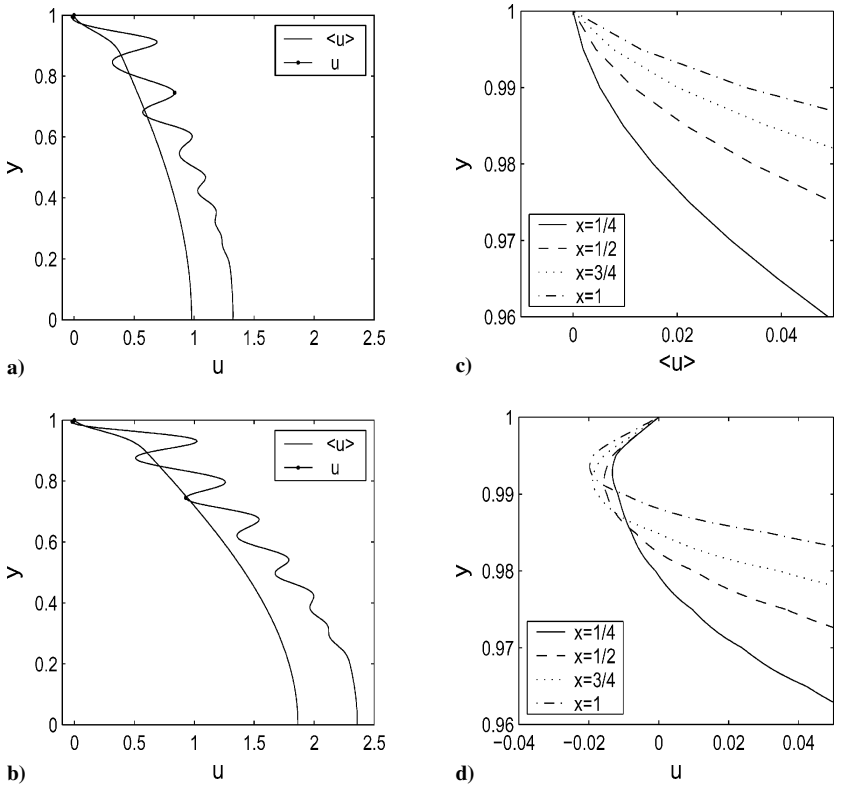

Fig. 18 Transverse variation of axial velocity for $\omega = 1$, $\varepsilon = 0.4$, $\delta = 20$, $M = 0.02$, $n = 1$ and $Re = 4 \times 10^5$ at $x =$ a) 0.5 and b) 1.0, when $t = 40$; c) near-wall results for axial velocity $\langle u \rangle$, and d) instantaneous axial velocity u for four axial locations.

small-scale disturbances within the channel flow for the Reynolds numbers considered.

The numerical solutions, characterized by distinct spatial structures on a scale small compared to the channel height H' and roughly quasi-periodic transients, can be split into mean and fluctuating parts. Here, the objective is to evaluate the rms intensity and the Reynolds stress, as well as to compare the mean and instantaneous axial speed distributions. Data for the parameter set $M = 0.02$, $Re = 4 \times 10^5$, $\varepsilon = 0.4$, $n = 1$, $\omega = 1$, and $t \leq 40$ are used. It is understood that the means and fluctuations are only characteristics of this data set because the solution is not quasi steady during the entire time interval.

A methodology borrowed from the asymptotic analysis by Zhao et al.[2] and used previously in the computational context by Kirkkopru et al.[3,6] is employed to divide axial and transverse transient velocities into mean motion and fluctuations:

$$u = \langle u \rangle + u'_p + u'_r \tag{20}$$

$$v = \langle v \rangle + v'_r \tag{21}$$

where u'_p is the acoustic fluctuation, u'_r and v'_r are the rotational fluctuations, and $\langle\ \rangle$ denote standard time averaging.[39]

If $u' \equiv u'_p + u'_r$, then the rms values of the axial and transverse fluctuation intensities are defined by

$$\sqrt{\langle u'u' \rangle} = \sqrt{\langle u'_p u'_p \rangle + 2\langle u'_p u'_r \rangle + \langle u'_r u'_r \rangle} \tag{22a}$$

$$\sqrt{\langle v'v' \rangle} = \sqrt{v'_r v'_r} \tag{22b}$$

Equation (22a) contains purely acoustic and rotational terms, as well as a product of both fluctuations.

Figures 18a and 18b show the transverse variations of the time-averaged mean flow $\langle u \rangle$ and the instantaneous axial velocity u in Eq. (20) for $t = 40$ at $x = 0.5$ and the exit plane $x = 1$. The mean velocity profile has a relatively steep gradient near the wall and differs in shape from the Culick[38] and steady-flow profiles observed in Fig. 1. This effect arises from momentum transport by Reynolds stresses near the injection surface $y = 1$, shown later. The smooth shape of the mean flow near $y = 1$ does not hint at the local spatial variations present in the instantaneous profiles. For example, the comparison of mean and instantaneous values close to the injection surface in Figs. 18c and 18d show very significant differences between the profiles, including reverse flow in the latter. Similar comparisons at other values of time show that the instantaneous wall gradient fluctuates between positive and negative values. Qualitatively similar results are observed in the asymptotic studies.[8]

Figure 19 shows the transverse and axial distribution of the rms fluctuation intensity of the axial velocity in the chamber, as defined in Eq. (22), where the result is decomposed into three parts: acoustic, $\langle u'_p u'_p \rangle$; acoustic–rotational, $\langle u'_p u'_r \rangle$; and rotational, $\langle u'_r u'_r \rangle$. The ramplike surface near the centerline exhibits the contribution from the acoustic term because the vorticity generated at the sidewall has convected out to about $y = 0.2$ by $t = 40$. The wrinkles represent the contribution from rotational effects and are of a similar magnitude to those arising from acoustics. Note that the peak amplitude increases and moves gradually toward the sidewall with increasing axial distance downstream.

The axial and transverse variations of the Reynolds stress, obtained from the time average of the mixed product of the velocity fluctuation $\langle u'v' \rangle$ are shown in Fig. 20. This product represents the transport of axial momentum through a surface normal to the y axis. The stress has significant negative values adjacent to the wall near $x = 0.5$ and decreases in amplitude with distance from the injection surface. The near-wall portion of the mean velocity in Figs. 18a and 18b results from the relatively large Reynolds stresses present there. The presentation of the data in terms of mean and fluctuating contributions provides further insight into the channel flow properties in terms often used to analyze quasi-steady flows.

More traditional numerical simulations of vorticity and turbulence in channel flows with wall injection are reviewed by Chaouat.[44] New solutions to the time-dependent Navier–Stokes equations with a Reynolds stress turbulent model are presented. The boundary conditions on the injection surface consist of a steady transverse

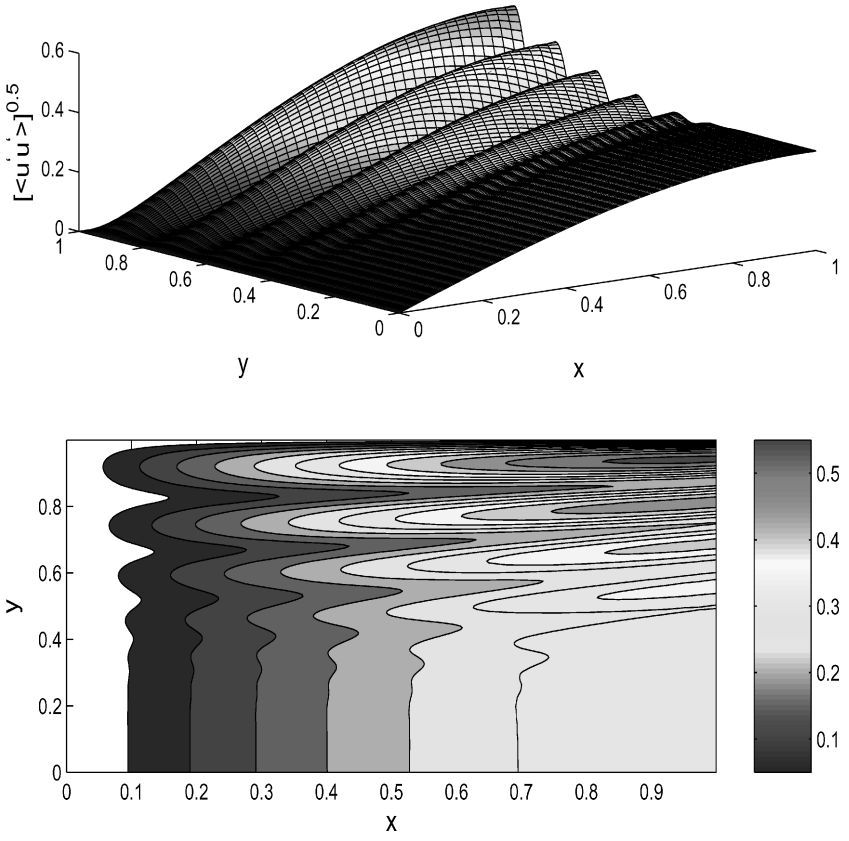

Fig. 19 RMS intensity of axial velocity $\langle u'^2 \rangle^{0.5}$ at $t = 40$.

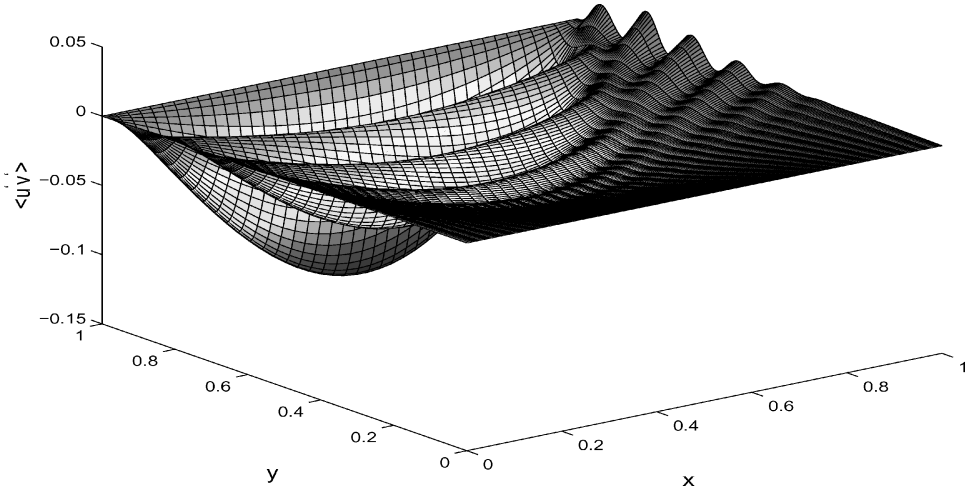

Fig. 20 Time average of $\langle u'v' \rangle$ at $t = 40$.

velocity and pseudoturbulence defined in terms of prescribed levels of Favre-averaged transverse kinetic energy fluctuations. Transition on the injection surface is observed to occur far downstream in the channel at a location sensitive to the level of psuedoturbulence. Mean axial velocity profiles are basically laminar until about halfway down the channel and then show signs of transition. None of the acoustic-related effects discussed in the present work are seen in Chaouat's results. For example, upstream in the channel, wall generated vorticity seen in Figs. 14–17 is not present, implying that the vorticity generating mechanism discussed in the present work is not locally operative. Note that the transient injection wall boundary conditions used in the present analysis are quite different from those in Chaouat's work, and so a quantitative comparison of results is not possible. In contrast, one finds in both types of studies intense vorticity located adjacent to the injection wall. It is difficult to know from the turbulent theory results if the source of the downstream vorticity is classical transition to turbulence, or partly the result of the kind of mechanism discussed in this paper. A related, more recent study by Yuksel et al.[45] employs the shear-stress transport k–ω methodology to capture axial velocity and turbulent kinetic energy distributions for the same channel configuration used by Chaouat.

Conclusions

Numerical solutions to the parabolized compressible flow equations, including transport effects, are used to describe acoustically active internal flow in a channel. Heat transfer, temperature, and

vorticity dynamics, caused by transient sidewall mass addition of a constant temperature gas, are quantified. An accurate representation of wave reflections at boundaries has facilitated accurate acoustic velocity and vorticity distributions in the low-Mach-number and large-Reynolds-number flow.

The computational results validate concepts derived from asymptotic theory.[8] After the transient sidewall injection is initiated, the acoustic pressure disturbance interacts with the constant temperature injected fluid to generate a relatively large transverse temperature gradient at the sidewall. For appropriate ranges of Reynolds number, Mach number, and frequency, the temperature waves are transported into the chamber by the transverse velocity component of the flowfield.

The amplitude and the wavelength of the spatial oscillations near the injection surface are generally larger than those away from the wall. Although the temperature variations in the flowfield are relatively small, one finds that the temperature gradients are much larger. These results are in excellent qualitative agreement with the asymptotic predictions by Staab et al.[8] and in earlier related work by Zhao et al.[2] In addition, the time history of the temperature and its gradient show that forced and eigenfunction modes coexist as predicted in the asymptotic analyses.[8]

Vorticity contour plots show that several spatial waves of vorticity are found across the chamber with the largest values occurring near the sidewall. The largest shear stresses appear at downstream locations for $n = 1$. For $n = 3$ and 5, many of vorticity contours are closed. The variation in the amplitude with the axial direction is nonmonotonic, in contrast to the results for $n = 1$ when only an increase occurs in the downstream direction. As the wave number index n increases, the vorticity amplitudes decrease, the result of diminished acoustic disturbance amplitudes. Although not shown, similar results pertain to the temperature field.

The relatively large sidewall temperature gradient implies that there is unexpected sidewall heat transfer even with constant temperature injection. Similarly, the amplitude of the nondimensional intensive transient vorticity is larger than the velocity disturbance, as predicted originally by Zhao et al.[2] As a consequence, the sidewall shear stress is considerably larger than that of Culick's steady solution[38] in Eq. (10). A comparison of mean flow and fluctuating flow properties, including rms values, provides another opportunity to observe the presence of relatively large, oscillatory transverse velocity gradients, for example, shear stresses, acting on the sidewall.

Experiments involving transient vorticity generation at an injection surface have been described recently by Vetel et al.[26,27] Although the geometrical configuration differs substantially from that in the present work, the conceptual perspective regarding vorticity pattern generation by an interaction between the imposed pressure gradient distribution and the injected fluid is supportive of the modeling effort conclusions.

It can be conjectured that the results described here may help to identify high heat transfer and erosional burning locations in solid rocket motor chambers. An understanding of oscillatory, intense axial shear stress and heat transfer on the sidewall will be useful for developing physically viable boundary conditions at the decomposing interface of a burning solid propellant. The interesting idea here is to account for the scouring effect of oscillatory shear stress on the fizz–foam zone thought to exist at the gas–propellant interface. Although the axial velocity in the combustion zone may be small, the results of the present study suggest that the velocity gradient will be relatively large and, hence, can be a source of axial deformation and perhaps stripping of easily deformable surface material. An application of the concepts prescribed in this work is anticipated in the near future.

Acknowledgments

Support from the U.S. Air Force Office of Scientific Research and the patience of Mitat Birkan are appreciated. In addition, the first author acknowledges postdoctoral support from the Center for Simulation of Advanced Rocket and the Aeronautical and Astronautical Engineering Department at the University of Illinois at Urbana–Champaign, where an earlier draft of this paper was written. The first author also thanks the Mechanical Engineering Department at the University of Colorado for hospitality during an extended research visit. A substantial discussion with A. Sileem of Menoufia University, Shebin El-Kom, Egypt, is appreciated.

References

[1]Zhao, Q., "Nonlinear Acoustic Processes in Solid Rocket Engines," Ph.D. Dissertation, Mechanical Engineering Dept., Univ. of Colorado, Boulder, CO, Aug. 1994.

[2]Zhao, Q., Staab, P. L., Kassoy, D. R., and Kirkkopru, K., "Acoustically Generated Vorticity in an Internal Flow," *Journal of Fluid Mechanics*, Vol. 413, 1999, pp. 247–285.

[3]Kirkkopru, K., Kassoy, D. R., and Zhao, Q., "Unsteady Vorticity Generation and Evolution in a Model of a Solid Rocket Motor," *Journal of Propulsion and Power*, Vol. 12, No. 4, 1996, pp. 646–654.

[4]Staab, P. L., and Kassoy, D. R., "Three Dimensional, Unsteady, Acoustic-shear Flow Dynamics in a Cylinder with Sidewall Mass Addition," *Physics of Fluids*, Vol. 9, No. 12, 1997, pp. 3753–3763.

[5]Staab, P. L., Zhao, Q., Kassoy, D. R., and Kirkkopru, K., "Co-Existing Acoustic-Rotational Flow in a Cylinder with Axisymmetric Sidewall Mass Addition," *Physics of Fluids*, Vol. 11, No. 10, 1999, pp. 2935–2951.

[6]Kirkkopru, K., Kassoy, D. R., Zhao, Q., and Staab, P. L., "Acoustically Generated Unsteady Vorticity Field in a Long Narrow Cylinder with Sidewall Injection," *Journal of Engineering Mathematics*, Vol. 42, 2002, pp. 65–90.

[7]Staab, P. L., and Kassoy, D. R., "Three-dimensional Acoustic-Rotational Flow in a Cylinder with Sidewall Mass Addition," *Physics of Fluids*, Vol. 14, No. 9, 2002, pp. 3141–3159.

[8]Staab, P. L., Rempe, M. J., and Kassoy, D. R., "Acoustic-Rotational Internal Flow Caused by Transient Sidewall Mass Addition," *SIAM Journal on Applied Mathematics*, Vol. 65, No. 2, 2004, pp. 587–617.

[9]Cole, J. D., and Aroesty, J., "The Blowhard Problem: Inviscid Flows with Surface Injection," *International Journal of Heat and Mass Transfer*, Vol. 11, No. 7, 1968, pp. 1167–1182.

[10]Culick, F. E. C., and Yang, V., "Nonsteady Burning and Combustion Stability of Solid Propellants," *Prediction of the Stability of Unsteady Motions in Solid-Propellant Rocket Motors*, edited by L. De Luca, E. W. Price, and M. Summerfield, Vol. 143, Progress in Astronautics and Aeronautics, AIAA, Washington, DC, 1992, pp. 719–779.

[11]Flandro, G. A., "Solid Propellant Acoustic Admittance Corrections," *Journal of Sound and Vibration*, Vol. 36, No. 3, 1974, pp. 297–312.

[12]Flandro, G. A., "Effects of Vorticity on Rocket Combustion Stability," *Journal of Propulsion and Power*, Vol. 11, No. 4, 1995, pp. 607–625.

[13]Majdalani, J., and Van Moorhem, W., "Multiple-Scales Solution to the Acoustic Boundary Layer in Solid Rocket Motors," *Journal of Propulsion and Power*, Vol. 13, No. 2, 1997, pp. 186–193.

[14]Majdalani, J., and Van Moorhem, W., "Improved Time-Dependent Flowfield Solution for Solid Rocket Motors," *AIAA Journal*, Vol. 36, No. 2, 1998, pp. 241–248.

[15]Majdalani, J., and Rienstra, S. W., "Two Asymptotic Forms of the Rotational Solutions for Wave Propagation Inside Viscous Channels with Transpiring Walls," *Quarterly Journal of Mechanics and Applied Mathematics*, Vol. 55, No. 1, 2002, pp. 141–162.

[16]Majdalani, J., and Flandro, G. A., "The Oscillatory Pipe Flow with Arbitrary Wall Injection," *Proceedings of the Royal Society of London, Series A: Mathematical and Physical Sciences*, Vol. 458, No. 2023, 2002, pp. 1621–1651.

[17]Flandro, G. A., and Majdalani, J., "Aeroacoustic Instability in Rockets," *AIAA Journal*, Vol. 41, No. 3, 2003, pp. 485–497.

[18]Casalis, G., Avalon, G., and Pineau, J. P., "Spatial Instability of Planar Channel Flow with Fluid Injection Through Porous Walls," *Physics of Fluids*, Vol. 10, No. 10, 1998, pp. 2558–2568.

[19]Venugopal, P., Najjar, F. M., and Moser, R. D., "DNS and LES Computations of Model Solid Rocket Motors," AIAA Paper 2000-3571, July 2000.

[20]Venugopal, P., Najjar, F. M., and Moser, R. D., "Numerical Simulations of Model Solid Rocket Motor Flows," AIAA Paper 2001-3950, July 2001.

[21]Vuillot, F., and Avalon, G., "Acoustic Boundary Layers in Solid Propellant Rocket Motors Using Navier–Stokes Equations," *Journal of Propulsion and Power*, Vol. 7, No. 2, 1991, pp. 231–239.

[22]Vuillot, F., "Vortex-Shedding Phenomena in Solid Rocket Motors," *Journal of Propulsion and Power*, Vol. 11, No. 4, 1995, pp. 626–639.

[23]Lupoglazoff, N., and Vuillot, F., "Numerical Simulations of Parietal Vortex-Shedding in a Cold Flow Setup," AIAA Paper 98-3220, July 1998.

[24]Tseng, C. F., Tseng, I. S., Chu, W., and Yang, V., "Interaction Between Acoustic Waves and Premixed Flames in Porous Chamber," AIAA Paper 94-3328, June 1994.

[25]Roh, T. S., and Yang, V., "Transient Combustion Responses of Solid Propellants to Acoustic Disturbances in Rocket Motors," AIAA Paper 95-0602, Jan. 1995.

[26]Vetel, J., Plourde, F., Kim, S. D., and Guery, J.-F., "Numerical Simulations of Wall and Shear Layer Instabilities in a Cold Flow Setup," *Journal of Propulsion and Power*, Vol. 19, No. 2, 2003, pp. 297–306.

[27]Vetel, J., Plourde, F., and Kim, S. D., "Amplification of a Shear-Layer Instability by Vorticity Generation at an Injecting Wall," *AIAA Journal*, Vol. 42, No. 1, 2004, pp. 35–46.

[28]Poinsot, T. J., and Lele, S. K., "Boundary Conditions for Direct Simulations of Compressible Viscous Flows," *Journal of Computational Physics*, Vol. 101, No. 1, 1992, pp. 104–129.

[29]Wu, T. Y., "Small Perturbations in the Unsteady Flow of a Compressible, Viscous and Heat Conducting Fluid," *Math and Physics*, Vol. 35, No. 1, 1956, pp. 13–27.

[30]Lagerstrom, P. A., "Laminar Flow Theory," *Theory of Laminar Flows*, edited by F. K. Moore, Princeton Univ. Press, Princeton, NJ, 1964, Sec. B, pp. 90 and 203.

[31]Landau, L., and Lifshitz, E. M., *Fluid Dynamics*, Addison Wesley Longman, Reading, MA, 1959, p. 293.

[32]MacCormack, R. W., "The Effect of Viscosity in Hypervelocity Impact Crating," AIAA Paper 69-354, April 1969.

[33]Gottlieb, D., and Turkel, E., "Dissipative Two-Four Methods for Time-Dependent Problems," *Mathematics of Computation*, Vol. 30, No. 136, 1976, pp. 703–723.

[34]MacCormack, R. W., "Numerical Method for Solving the Equations of Compressible Viscous Flow," *AIAA Journal*, Vol. 20, No. 9, 1982, pp. 1275–1281.

[35]MacCormack, R. W., and Baldwin, B. S., "A Numerical Method for Solving the Navier–Stokes Equations with Application to Shock–Boundary Layer Interaction," AIAA Paper 75-1, Jan. 1975.

[36]Thompson, K. W., "Time Dependent Boundary Conditions for Hyperbolic Systems," *Journal of Computational Physics*, Vol. 68, No. 1, 1987, pp. 1-24.

[37]Thompson, K. W.,"Time Dependent Boundary Conditions for Hyperbolic Systems Π," *Journal of Computational Physics*, Vol. 89, No. 2, 1990, pp. 439–461.

[38]Culick, F. E. C., "Rotational Axisymmetric Mean Flow and Damping of Acoustic Waves in a Solid Propellant Rocket," *AIAA Journal*, Vol. 4, No. 8, 1966, pp. 1462–1464.

[39]Hegab, A. M., "A Study of Acoustic Phenomena in Solid Rocket Engines," Ph.D. Dissertation, Mechanical Power Engineering Dept., Menoufia Univ., Shebin El-Kom, Egypt, March 1998.

[40]Balakrishnan, G., Liňan, A., and Williams, F. A., "Compressibility Effects in Thin Channels with Injection," *AIAA Journal*, Vol. 29, No. 12, 1991, pp. 2149–2154.

[41]Smith, T. M., Roach, R. L., and Flandro, G. A., "Numerical Study of the Unsteady Flow in a Simulated Solid Rocket Motor," AIAA Paper 93-0112, Jan. 1993.

[42]Liou, T. M., and Lien, W. Y., "Numerical Simulations of Injection Driven Flow in a Two-Dimensional Nozzleless Solid Rocket Motor," *Journal of Propulsion and Power*, Vol. 11, No. 4, 1995, pp. 600–606.

[43]Hegab, A. M., Kassoy, D. R., and Sileem, A. A., "Numerical Investigation of Acoustic–Fluid Dynamics Interaction in an SRM Chamber/Nozzle Model," AIAA Paper 98-0712, Jan. 1998.

[44]Chaouat, B., "Numerical Simulations of Channel Flows with Fluid Injection Using Reynolds Stress Model," AIAA Paper 2000-0992, Jan. 2000.

[45]Yuksel, U. G., Sen, B. A., and Kirkkopru, K., "Computation of Flow Inside a Channel with Sidewall Mass Injection using Various Turbulence Models," Proceedings of the 4th International Conf. on Computational Heat and Mass Transfer, ICCHMT'05-296, May 2005.

M. Sichel
Associate Editor